Experiments in Fluids (2021) 62:99
https://doi.org/10.1007/s00348-021-03191-x

RESEARCH ARTICLE

Application of femtosecond-laser tagging for unseeded velocimetry in a large-scale transonic cryogenic wind tunnel

Daniel T. Reese[1] · Ryan J. Thompson[2] · Ross A. Burns[3] · Paul M. Danehy[1]

Received: 23 December 2020 / Revised: 12 March 2021 / Accepted: 21 March 2021

Abstract

Femtosecond laser electronic excitation tagging (FLEET) velocimetry was applied in the National Transonic Facility and assessed for its use in providing quantitative velocity measurements in a large-scale cryogenic wind tunnel. Comparisons of freestream results with theory and existing tunnel measurements indicate that FLEET velocity measurements agree within 1% of the tunnel reference, while the largest error among all conditions remained within 2.5%. For single-shot velocity measurements, binning of the FLEET intensity data improved the signal-to-noise ratio sufficiently to provide measurement precisions on the order of 1% of the freestream velocity. After confirmation of system performance, spatially resolved velocity profile measurements were obtained in the wake downstream of the Common Research Model wing. Effects of the model angle-of-attack on velocity deficit profiles were explored, and a two-dimensional, one-component velocity map resolving the wake region was constructed by scanning the laser's position within the test section. The experimental campaign described herein represents the first non-intrusive, quantitative measurements of velocity made in this facility since its inception in 1984.

✉ Daniel T. Reese
daniel.reese@nasa.gov

Paul M. Danehy
paul.m.danehy@nasa.gov

[1] NASA Langley Research Center, Hampton, USA

[2] University of Virginia, Charlottesville, USA

[3] National Institute of Aerospace, Hampton, USA

Published online: 17 April 2021

Graphic abstract

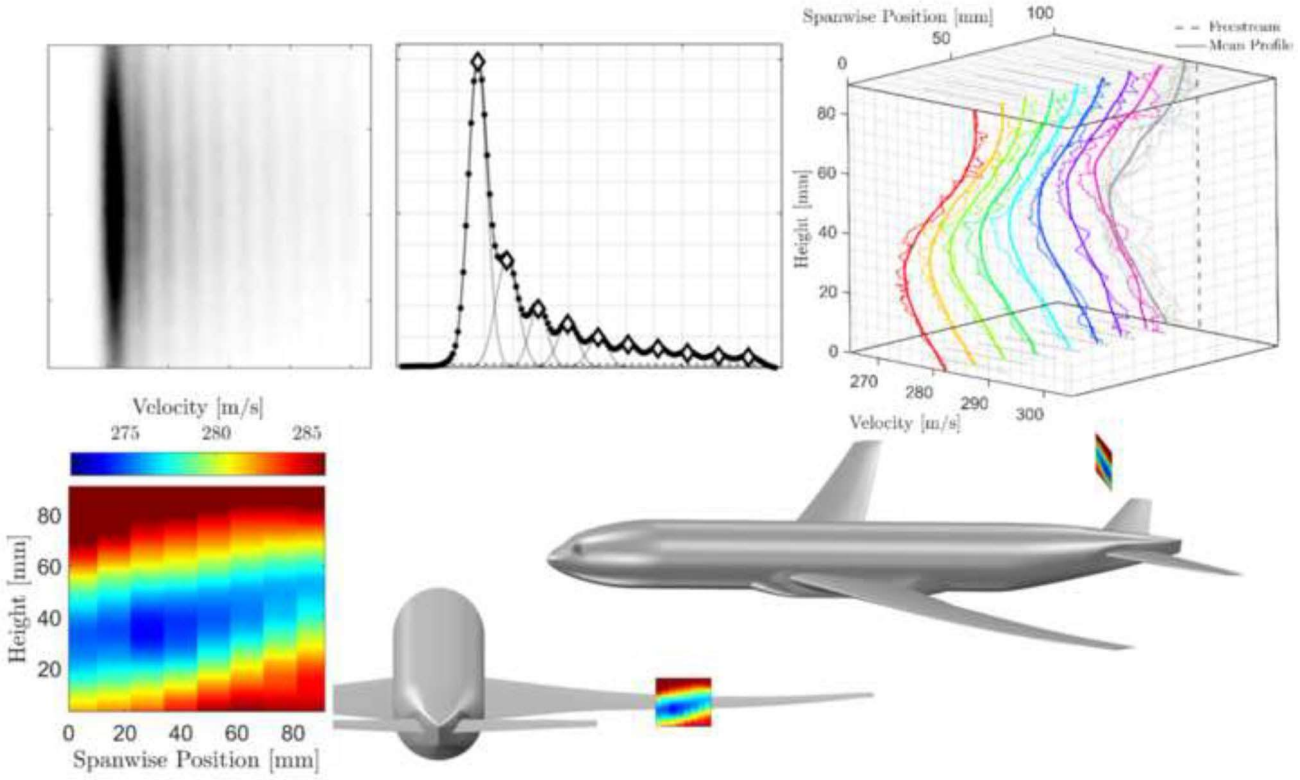

1 Introduction

Quantitative measurements of off-body flow phenomena remain an indispensable asset necessary for the successful development and continued improvement of aerospace flight vehicles (Babuska and Oden 2004; Cosner 1998). Experiments providing data at flight-accurate Reynolds numbers are especially valuable to these efforts, as they provide insight into aerodynamic effects that the vehicle will experience in flight. Moreover, the data engendered by these experiments can serve to constrain aerodynamic and turbulence models, as well as expand the existing experimental databases that are increasingly relied upon by the computational fluid dynamics (CFD) community (Clark et al. 2020; Oberkampf and Trucano 2000, 2002; Oberkampf and Barone 2004). Despite the importance of these facilities and the measurements made therein, quantitative, off-body measurements in this flow regime remain limited, while non-intrusive measurements are rarer still.

One reason for the lack of these vital datasets is the inability of most test facilities to operate at flight-relevant conditions; however, a class of wind tunnels known as transonic cryogenic tunnels (TCTs) were developed to allow for ground testing at flight-accurate Reynolds and Mach numbers (Goodyer 1992; Wegener 1991). TCTs are capable of accessing this flow regime by creating a low-temperature, high-pressure environment within the wind tunnel through the injection of cryogenic nitrogen, which simultaneously increases the density and decreases the dynamic viscosity of the flow (Ladson and Ray 1987; Snow et al. 1982, 1987). In order to produce and contain these frigid temperatures, extreme pressures, and high-speed flows, TCTs require a sturdy construction traditionally lacking in optical access to the test section. Coupled with effects such as tunnel vibrations, frost accumulation, and thermal expansion and contraction of the facility, TCTs offer a harsh environment not amenable to the sensitive instruments often used to provide the detailed measurements requested by wind tunnel customers.

To help reduce the barrier-to-entry associated with testing at such extreme conditions, small-scale TCTs [such as the Cryogenic Wind Tunnel Cologne in Germany (Viehweger 1989) and the NASA 0.3-meter TCT in Virginia (Kilgore 1976; Ray et al. 1979)] are often utilized as pilot facilities where measurement techniques can be assessed for their applicability in the cryogenic environment more quickly and

cheaply than in the corresponding full-scale facilities—the European Transonic Windtunnel (ETW) (Green and Quest 2011) and the National Transonic Facility (NTF) (Foster and Adcock 1996; Fuller 1981; Wahls 2001), respectively. Despite mitigating some select issues associated with testing under such unfavorable conditions, the difficulties inherent to even small-scale TCTs impede the application of nearly every measurement technique, preventing many researchers from ever attempting measurements given the unforgiving environment. These hostile testing conditions are yet another reason that quantitative datasets are lacking in this regime.

Undeterred by the appreciable challenges, several researchers have overcome significant obstacles in order to implement unique solutions that provide valuable off-body measurements in TCTs. Some measurement techniques applied in the 0.3-m TCT including laser Doppler velocimetry (Gartrell et al. 1981), laser transit anemometry (Honaker and Lawing 1985), schlieren (Gartenberg et al. 1994), and shadowgraphy (Snow et al. 1987) were determined to be unsuitable for application in NTF and never saw use at the full-scale facility. Other methods, however, such as Rayleigh scattering (Burns et al. 2016b; Herring and Shirinzadeh 2002; Shirinzadeh et al. 1999) showed sufficient success in the 0.3-m TCT to be attempted in subsequent tests at the NTF (Herring et al. 2015). This foundational work also demonstrated that naturally occurring particles exist in both NTF and the 0.3-m TCT despite programmatic restrictions banning active "seeding" of the flow. The purposeful introduction of tracer particles, droplets, or vapor into NASA TCTs is prohibited due to the contaminant's ability to damage sensitive wind tunnel components and condense on test models, introducing unwanted surface roughness (Couch et al. 2010). These regulations currently preclude the application of conventional particle-based methods in NASA-owned cryogenic wind tunnels, and resultantly, off-body flow measurements have traditionally been provided by a survey rake containing various temperature, velocity, and pressure probes (King et al. 2014). However, an investigation exploring the potential of using the naturally occurring seed as a flow-tracer for velocimetry is currently underway and may provide a solution permitting the implementation of advanced off-body measurement techniques previously thought inapplicable in these wind tunnels (Retter et al. 2021). At the European TCTs, where introduction of particles is not prohibited, more traditional velocimetry methods such as particle image velocimetry (PIV) (Fey et al. 2010; Germain and Quest 2005; Konrath et al. 2015; Lutz et al. 2013; Quest and Konrath 2011; Waldmann et al. 2016) and Doppler global velocimetry (DGV) (Willert et al. 2005) have been successfully employed to provide two-dimensional, multi-component velocity measurements.

With the recent emergence of a new class of molecular tagging velocimetry (MTV) techniques known as laser electronic excitation tagging (LEET) came a novel and elegant solution for obtaining unseeded, quantitative, off-body measurements of velocity in large-scale TCTs. The LEET method of velocimetry utilizes a focused laser pulse to dissociate and ionize molecular nitrogen; upon recombination, the tagged gas fluoresces and can be tracked using sequential imaging (Li et al. 2019). LEET-based velocimetry methods are particularly well suited for application in TCTs, not only due to the measurement's reliance on nitrogen (making them unseeded techniques in the pure nitrogen environment of a cryogenic wind tunnel), but also because the signal intensity improves with increasing density (Burns et al. 2018a, b; Reese et al. 2020), so the high-pressure, low-temperature conditions under which TCTs operate is favorable. This family of measurements includes the "standard" femtosecond LEET (FLEET) (Danehy et al. 2014; DeLuca et al. 2014; Edwards et al. 2015; Limbach and Miles 2017; Michael et al. 2011; Peters et al. 2019; Zhang et al. 2018; Zhang and Miles 2018), a high-repetition rate version employing a pulse-burst picosecond laser (PLEET) (Jiang et al. 2017), and a less thermally perturbative method known as selective two-photon absorptive resonant FLEET (STARFLEET) (Jiang et al. 2016a, b, c). Each of these techniques has been proven to provide non-intrusive quantitative measurements of flow velocity in the 0.3-m TCT (Burns and Danehy 2017a, b; Burns et al. 2015, 2016a, b, 2018a, b; Reese et al. 2018, 2019, 2020), but none had been successfully adapted for use in large-scale TCTs until the application of FLEET in NTF as described in this report.

The present work details a two-part experimental campaign in which FLEET was implemented to provide the first non-intrusive, quantitative velocity measurements in NTF. The research described herein satisfies a call for off-body velocimetry in NASA's large-scale TCT that had remained unanswered since the facility's inception in 1984 (Hunter et al. 1982; Wahls 2001). As detailed below, initial velocity measurements were made over a range of flow conditions at a single location in the freestream ahead of a survey rake. This permitted comparison of FLEET results with both theory and existing facility measurements of velocity in order to determine the applicability of this technique in a large-scale TCT. Following the first successful implementation of FLEET in NTF, measurement system upgrades allowed for spatial scanning of the laser in the second entry; this added capability provided quantitative, two-dimensional, one-component velocity measurements downstream of the Common Research Model (CRM) wing. The following section describes the experimental setup employed to produce and image the FLEET signal within the NTF test section, while Sect. 3 discusses the data processing used to calculate flow velocity from raw data. Results are presented in Sect. 4, before an in-depth discussion of their significance and a note on the potential impact of this new measurement system

in Sect. 5. Finally, important findings are summarized and conclusions are drawn in Sect. 6.

2 Experimental setup

This section describes the three main systems (as well as the various subsystems and the interplay between them) that were employed to yield the FLEET velocimetry results discussed throughout the remainder of this article. Section 2.1 provides an overview of the relevant details of the NTF wind tunnel facility. Information regarding the "write system" used to deliver the laser beam and produce the FLEET signal within the measurement region is given in Sect. 2.2, while Sect. 2.3 outlines the "read system" implemented to capture the raw FLEET emission data that were used to calculate flow velocity.

2.1 The National Transonic Facility

The NTF is a fan-driven, closed-circuit, continuous-flow TCT located at NASA Langley Research Center in Hampton, Virginia. Though this facility is capable of operating at temperatures up to 340 K using air as the test gas, the wind tunnel was designed to use high-pressure, cryogenic nitrogen to reach unit Reynolds numbers exceeding 4.2×10^8 m^{-1} in order to duplicate true-flight aerodynamics (Foster and Adcock 1996). These large Reynolds numbers are achieved by operating at temperatures as low as 116 K, total pressures up to 860 kPa, and Mach numbers ranging from approximately 0.1 to 1.2 (Fuller 1981). The NTF has a double-walled construction, where an outer shell contains the high pressure environment, and an inner test section with slotted walls acts as the channel through which the test gas flows. The region between the test section walls and the outer pressure shell is known as the plenum. Prior to modifications made for this experimental campaign (as described further in the following subsection), there was no optical access through the outer pressure shell, and only a limited number of windows embedded within the test section walls, ceiling, and floor. Considered a large-scale facility, the NTF test section is 7.62 m long and has a 2.5 m square cross section following a 15:1 contraction in area; in fact, the low-speed diffuser section is sufficiently sizeable to fit the entire 0.3-m TCT facility (Retter et al. 2021). The tunnel is also equipped with a data acquisition system (DAS) that allows for the acquiring, processing, recording, and displaying of test data. Additional information regarding the NTF can be found in references Foster and Adcock (1996), Fuller (1981), and Wahls (2001).

While not permanent fixtures of the NTF, the survey rake and CRM models that were used during FLEET testing are considered part of the experimental facility in this work. The survey rake, which was in use during the freestream evaluation tests, has a double wedge airfoil shape, mounts to the wind tunnel model support structure, spans 2.1 m with a chord length of 28.9 cm and maximum thickness of 24 mm. Similar to that used in reference King et al. (2014), the rake has 21 ports for mounting probes with a 10.16 cm centerline-to-centerline spacing, and throughout the test, it would be rotated in six degree increments to allow for pressure, temperature, and velocity measurements along the tunnel cross section. A schematic of the survey rake is shown in Fig. 1a in the horizontal position along the centerline of the test section.

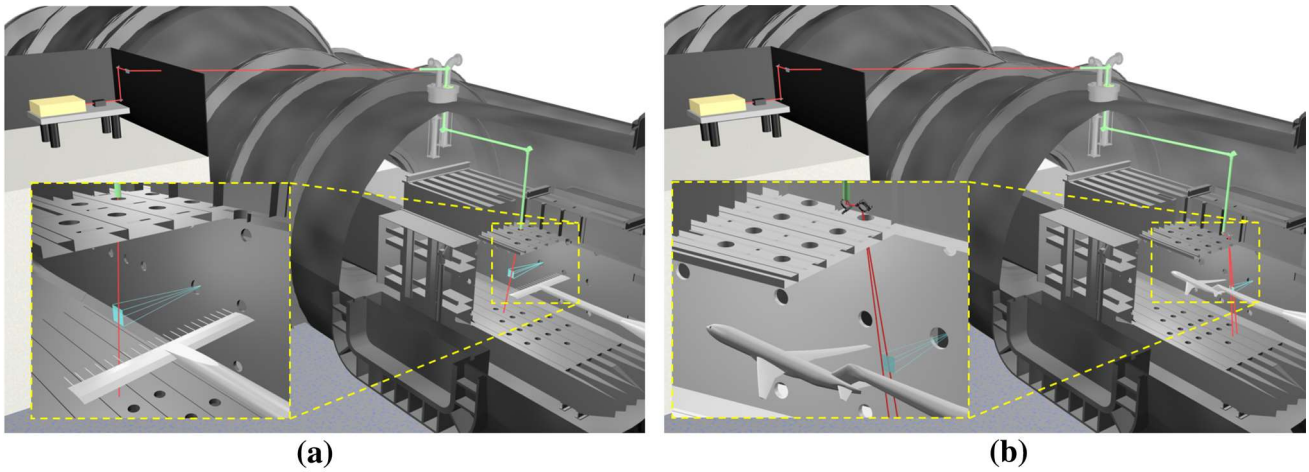

Fig. 1 Schematic of the NTF test section and the FLEET experimental setup used for **a** freestream measurements ahead of a survey rake, and **b** wake measurements downstream of the Common Research Model wing. The beam path is highlighted in red, the LPS is shown as green, and the camera field of view is indicated by the blue rectangle

The CRM used in the velocity wake surveys is a 2.7% scale model of a contemporary supercritical transonic wing and fuselage that is representative of a widebody commercial transport aircraft and, like the survey rake, was sting-mounted during testing. Designed for a cruise Mach number of 0.85 and a corresponding design lift coefficient of 0.5, the wing of the CRM has an aspect ratio of 9.0 with a leading edge sweep angle of 35°. The geometry used was the WBT0 (wing/body/tail = 0°) configuration. The wing reference area is 2796 cm^2, the wing span is 158.6 cm, and the aerodynamic chord is 18.9 cm. Additional information regarding the CRM can be found in reference (Vassberg et al. 2008), and a schematic of the CRM is shown in Fig. 1b along the centerline of the test section with an angle of attack of 2°. Due to the high power of the femtosecond laser and the potential for model damage, the location of the FLEET focal point relative to the proximity to the models was carefully considered and placed several centimeters away from both the rake and the CRM. To prevent the detection of potential disturbances in the flow caused by the FLEET signal, FLEET data were only taken after the survey rake and CRM teams had completed data collection.

2.2 Write system

A "write system" was developed to deliver femtosecond laser pulses to (and produce the FLEET signal within) the measurement region of the NTF test section. First described in reference Reese et al. (2019), the write system is made up of three main subsystems: the laser delivery system (LDS), laser penetration system (LPS), and optics system. The purpose of the LDS is to produce laser pulses of the desired power and beam diameter and deliver them to the LPS installed in the NTF wind tunnel roughly 10 m away. Located on a mezzanine far from the harsh conditions surrounding the TCT, the LDS is free from environmental disturbances associated with operation of the wind tunnel, including large vibrations, considerable temperature fluctuations, and excessive condensation. The LDS begins with a regeneratively amplified, Ti:Sapphire laser system (Spectra-Physics Solstice Ace) with a repetition rate of 1 kHz, pulse duration of 70 fs FWHM, center wavelength of 800 nm, spectral bandwidth of 13 nm FWHM, and maximum power output of 7 W. This high-power femtosecond laser is installed collinearly with an eye-safe continuous wave laser used for troubleshooting and the alignment of optics. Just beyond the laser aperture, an optical shutter is installed to only permit passage of the beam while acquiring velocity measurements. Laser power can be adjusted using a remotely controllable attenuator placed just after the optical shutter. Following the attenuator, a two-lens Galilean telescope is employed to increase the laser beam diameter, enabling a tighter focus in the test section and helping prevent damage to downstream optics.

Once the desired power and beam diameter have been attained, the light is directed to the height of the LPS entrance using a vertical periscope. The second mirror of this periscope also serves as the first mirror in a horizontal periscope oriented parallel to the wind tunnel, allowing for compensation of the tunnel expansion and contraction that occurs as run temperatures are changed. This adjustment for tunnel motion is achieved by housing the final mirror in a motorized mount which is, in turn, mounted on a remotely controlled translation stage. The motorized mirror allows for fine-scale adjustments to the angle that the beam enters the LPS, while the translation stage permits synchronized movement of the beam with the expanding or contracting tunnel without affecting the selected angular settings. The last mirror in the horizontal periscope is the final optic in the LDS and delivers the laser from the mezzanine to the LPS installed in the wind tunnel. By hiding a portion of laser safety curtain for this schematic, the LDS is visible on the mezzanine in the upper left corner of Fig. 1a, b. The laser is shown as a yellow box from which a red beam emanates. The black box just in front of the laser represents the shutter, attenuator, and telescope; the vertical and horizontal periscopes of the LDS are also clearly visible in this figure. It should be noted that although the red beam is shown for clarity in Fig. 1, before leaving the LDS, laser light is entirely enclosed in beam tubes to prevent intrabeam viewing of the laser on the mezzanine. After leaving the mezzanine, the beam propagates through free-space before entering the LPS (shown as green in Fig. 1a, b).

The LPS was designed to capture the femtosecond laser pulses delivered by the LDS, transfer them through the outer pressure shell of the wind tunnel, and preserve beam quality as the laser propagates through the plenum to the optics system. Comprised of four lengths of 2-inch diameter stainless steel pipe joined by three corner sections, the LPS provides an effective solution to the unfavorable conditions persistent throughout the TCT plenum. At each end of the series of pipe, anti-reflective-coated windows provide a seal so that a vacuum can be pulled within the LPS. The near-vacuum environment allows the laser beam to pass through the NTF plenum without degradation of beam quality by the high density atmosphere. The corner sections each contain a remotely controlled mirror (similar to the last mirror in the LDS) and a small video camera indicating the position of the laser beam on each mirror. Mirrors are positioned to ensure transmission of light into the facility and can be adjusted to account for beam drift in order to realign the laser within the LPS. At the exit of the LPS, the optics system directs the femtosecond pulses to the measurement region of the test section and focuses the laser beam to produce the FLEET signal.

In the first implementation of FLEET in the NTF, the LPS exit was positioned several centimeters above a window along the spanwise centerline of the tunnel, approximately 3.4 m downstream of the start of the test section. The optics system was attached to the window mount at the end of the LPS, directly inline with the final section of pipe and the center of the window in the test section ceiling. This first version of the optics assembly consisted of a focusing lens telescope used to create the FLEET signal near the center of the test section, and a 7° wedge prism. The prism was required to direct the beam upstream into the camera's field of view since the window in the ceiling through which the laser entered the test section was not aligned with the window in the side wall used to image the measurement region. Although it succeeded in producing FLEET emission in the desired location within the test section, the turning prism was detrimental to the fluorescence signal, cutting the intensity detected by the camera nearly in half compared with an optical assembly without the prism. Regardless, the original optics system used during initial FLEET testing provided the first-ever non-intrusive, quantitative velocimetry in NTF. These velocity measurements made in the freestream ahead of a survey rake serve as a proof-of-concept for the new system and a "checkout" of the FLEET technique in the NTF facility. The complete setup used for this first experimental campaign is shown in Fig. 1a.

Following the initial successful application of FLEET velocimetry in a large-scale TCT, modifications to the LPS and optics system provided higher quality data and introduced the ability to move the FLEET signal within the test section. In order to measure the wake flow induced by the CRM wing, the LPS exit was not only moved off the spanwise centerline, but also to a window approximately 1.2 m further downstream than the one used in the previous experiment. Additionally, the LPS exit was not placed directly above the test section window but was instead terminated at a location several centimeters upstream of the window. This positioning afforded the ability to replace the problematic wedge prism in the optics system used in the earlier studies with a pair of mirrors, the second of which was placed in a motorized mount similar to that used in the LDS and LPS. By adjusting the angles of this mirror, the beam was able to be scanned in both the spanwise and streamwise directions, though the FLEET signal location was only traversed in the spanwise direction for these studies. All upgrades made to the write system are reflected in Fig. 1b, which highlights the overall experimental setup used to provide CRM wake measurements in the second FLEET entry. The FLEET signal produced in the NTF test section by the write system in both campaigns was captured using a "read system" described in detail in the following subsection.

2.3 Read system

Just as the write system was used to produce the FLEET signal in the measurement region of the test section, a "read system" was developed to capture the FLEET emission used to calculate velocity. Imaging was done using a CMOS camera (Photron Mini AX-200) lens-coupled to a high-speed image intensifier (LaVision HS-IRO) with a Canon EF 135 mm *f*/2 objective lens. The camera and intensifier, as well as aperture and focus of the objective lens, were remotely adjustable in order to capture focused images as the FLEET signal was scanned along the spanwise direction of the test section. Although the camera was framed at 1 kHz to match the laser repetition rate (so that each frame contained FLEET signal from a single laser pulse), the intensifier was gated multiple times during a single camera exposure using a gate duration of 4 microseconds in order to capture multiple delayed exposures of the FLEET signal on a single frame. The number of intensifier gates per camera exposure and the time between gates were determined by the flow conditions; a slower freestream velocity necessitated longer delays between gates to avoid spatially overlapping FLEET signal, and approximately twice as many gates were able to be captured in nitrogen compared with using air as the test gas due to the longer-lived emission in pure N_2.

The imaging system was located inside the plenum, attached to the test section wall at the tunnel centerline height, where the FLEET signal could be viewed through a 20.3 cm diameter fused silica window. The camera field of view is shown in Fig. 1a, b as a blue rectangle projected back to the camera lens on the other side of the test section window. Because the plenum area is subject to the high pressure and low temperature environment present during tunnel operation, the intensified, high-speed camera system was placed inside of a cylindrical enclosure where the temperature and pressure could be regulated. The interior of the enclosure measures approximately 74 cm long by 33.5 cm in diameter, and heating was supplied by electrical resistance heaters, while cooling used during air mode operation was provided by cold purge air. The temperature and pressure were monitored remotely, and the pressure was maintained between 101 and 152 kPa, while the temperature stayed in a range between 289 and 326 K. The enclosure also contained a filter wheel that allowed different optical filters to be placed in front of the objective lens, and a network switch for communicating with the various components. Since the plenum area is inaccessible during testing and whenever the tunnel is in nitrogen mode, all components within the enclosure (as well as all subsystems encompassing the write system) were controllable using a unified system that permitted remote control of all components from the mezzanine, control room, and within the test section when tunnel access was permitted.

3 Data processing

Along with providing 2D velocity maps, 1D profiles, and 0D freestream measurements across a range of flow conditions, data captured during testing allowed for additional analysis providing insight into the performance of the technique, such as determining the FLEET signal lifetime as well as the accuracy and precision of measurements. Images obtained during testing underwent a multi-step processing routine to provide the results presented in Sect. 4, and each step of data processing is described in detail within this section. Sect. 3.1 covers the dewarping and calibration of raw data. Section 3.2 outlines the detection of peak FLEET intensity and the corresponding location of the signal. Section 3.3 discusses the calculation of velocity and lifetime from the peak signal position and intensity information.

3.1 Preprocessing

Before the start of each experimental campaign, a target consisting of black dots in a regular grid pattern was imaged to provide values for magnification and lens focus at several spanwise locations within the test section. By fitting these values at the calibration points, the requisite settings at any position along the camera field of view can be determined. The target was also used to correct FLEET data for perspective and lens distortions. This image correction was accomplished by using a custom centroid-finding algorithm to determine the dot locations, and then mapping each point to the expected location given the known target pattern. After determining the transformation at each measurement location in this way, the same transformation is then applied to FLEET image data in order to correct for perspective and lens distortions. Target calibration images also allow for the extraction of a scale factor used to bring pixels into physical units, since the spacing between dots is known. Once the images have been "dewarped" and scaled, each frame is rotated to an (x', y') coordinate system that orients the FLEET line vertically; this accounts for the laser entering the camera field of view at an angle. Next, a region of interest (ROI) containing the FLEET signal is determined for each valid frame of data. The position of the ROI was adjusted for each frame to account for motion of the FLEET signal between exposures resulting from LPS movements induced by the flow and wind tunnel vibrations. Note that, FLEET measurements in nitrogen had a sufficiently high signal-to-noise ratio (SNR) to provide single-shot results, meaning that a valid velocity measurement can be extracted from each of the 1000 frames of data obtained during the one second of data acquisition. However, data taken in air required time-averaging to increase SNR, thereby providing only a single valid ROI (and therefore velocity measurement) over the entire one second measurement timespan. The ROI is defined as the location of maximum average intensity in each of the x' and y' directions, plus and minus a chosen distance depending on flow conditions. Representative dewarped, scaled, and rotated ROIs for freestream FLEET data are shown in Fig. 2a–c for the single-shot nitrogen, time-averaged nitrogen, and time-averaged air cases, respectively. In these images, the dark lines indicate the FLEET signal exposed at several time delays, starting with the leftmost, darkest FLEET signal obtained 10 ns after the laser pulse. Subsequent exposures of the FLEET emission show a decaying signal that advects rightward with the flow. As shown in Fig. 2, a typical frame of data contains a total of 10 exposures in nitrogen, and 5 exposures in air.

3.2 Fitting FLEET intensity profiles

With the extraction of a preprocessed ROI from each valid frame of data, the next step in calculating velocity is detecting the peak signal for each FLEET line and the corresponding location of maximum intensity. This is accomplished by first binning the image in order to further increase the SNR, producing at least one intensity profile from each ROI. Although freestream data are binned into a single intensity profile (since there is no need for spatial resolution in the case of uniform flow), data obtained in the wake of the CRM are binned into multiple rows in order to obtain spatially resolved velocity profiles. In this subsection, only the simple case of a single profile is shown for the freestream data; additional processing used to obtain velocity profile measurements from FLEET signal images is discussed after providing further context in Sect. 4.

Measured freestream profiles are shown as dots for the single-shot nitrogen, time-averaged nitrogen, and time-averaged air cases in Fig. 2d–f, respectively. Each FLEET intensity profile is then modeled as a series of Gaussians on a DC offset,

$$I(x') = k_0 + \sum_{i=1}^{n} a_i \exp\left[-\left(\frac{x' - b_i}{c_i}\right)^2\right], \tag{1}$$

where k_o, a_i, b_i, and c_i are fit parameters, and n is determined by the number of exposures containing FLEET signal on the frame of interest. With this model of the FLEET profile, the location of peak intensity can be determined to sub-pixel accuracy. FLEET intensity models are displayed as solid lines fit to data in Fig. 2d–f; the calculated maximum intensities and corresponding locations are denoted by diamonds, while individual Gaussian fits are shown as dotted lines.

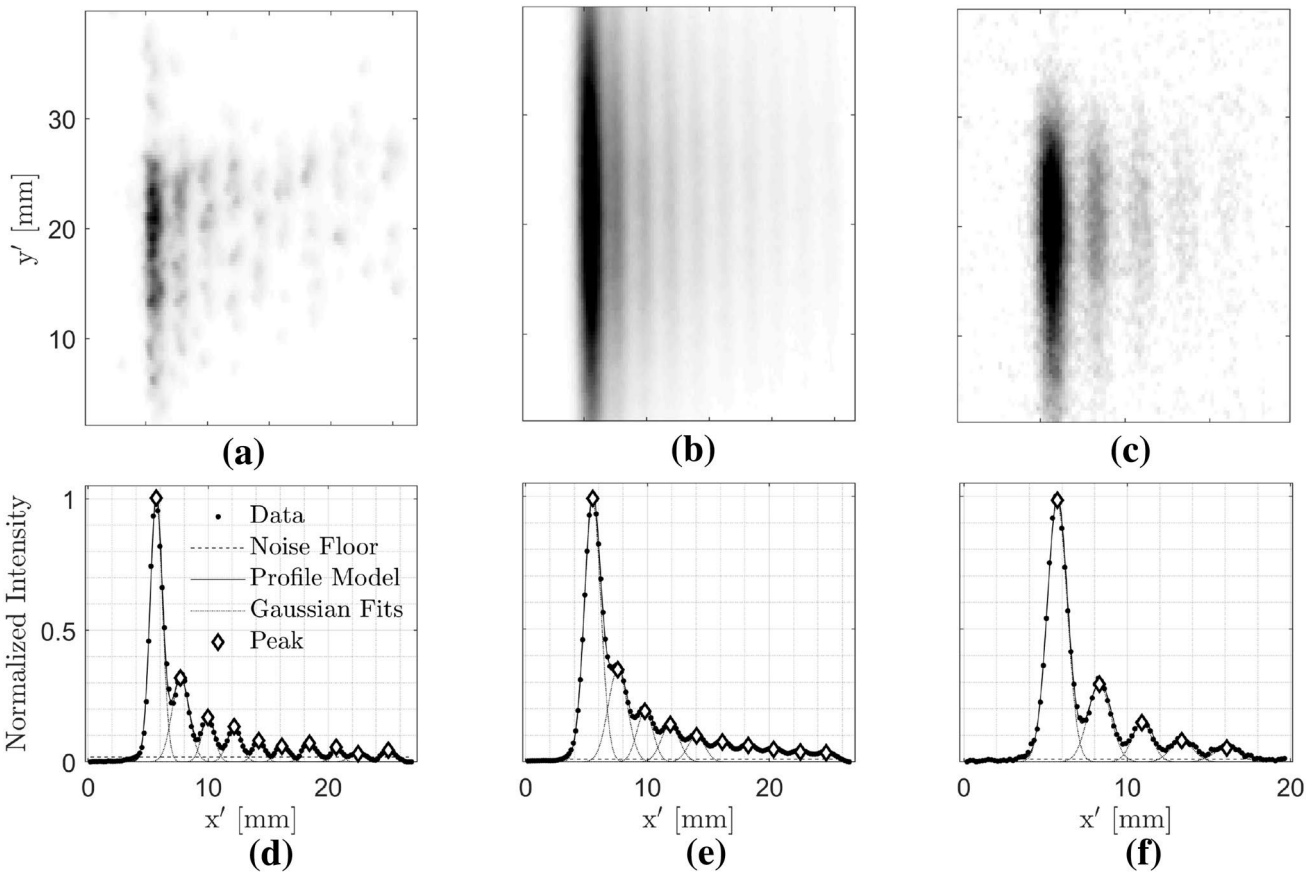

Fig. 2 Typical preprocessed regions of interest for the freestream **a** single-shot nitrogen, **b** time-averaged nitrogen, and **c** time-averaged air cases; the corresponding FLEET intensity profiles are shown in (**d–f**), respectively

Once the sub-pixel locations of the peak FLEET intensity have been determined, flow velocity and signal lifetime measurements can be extracted.

3.3 Signal lifetime and velocity measurements

Having determined the peak FLEET intensities at various time delays, as well as the corresponding locations to sub-pixel accuracy, the process for finding signal lifetime and flow velocity is relatively straightforward. Lifetime of the FLEET emission, which has important implications for making high-precision measurements, is calculated by first fitting the signal decay in time as a bi-exponential,

$$I(t) = ae^{bt} + ce^{dt}, \tag{2}$$

where I is the signal intensity, t is time, and a, b, c, d are fit parameters. This bi-exponential model is shown in Fig. 3a as a solid line fit to open diamonds representing peak intensity measurements. By designating the time when the laser pulse produces the FLEET signal as t_0, then the time that it takes for the signal intensity to reach $1/e$ of the initial value can be defined as the lifetime (τ); this lifetime measurement is indicated by a star in Fig. 3a. FLEET lifetime measurements such as these have been shown useful in measuring thermodynamic conditions under some circumstances (Edwards et al. 2015), and while lifetime measurements were not a primary focus of the current work, it should be noted that data quality was sufficient across all conditions for which velocity measurements were made to also enable the measurement of signal lifetime. Furthermore, the measured FLEET lifetimes in NTF were found to be consistent with previous findings from studies conducted in the 0.3-m TCT (Burns et al. 2018b).

Freestream velocity measurements in NTF are obtained by first fitting the location of peak intensity as a linear function of time. A linear relation between FLEET signal position and time is expected given that there is no acceleration in uniform freestream flow. Resultantly, the slope of the line fit using linear regression provides an estimate of velocity as $V' = \frac{\Delta x'}{\Delta t}$. Because this is the velocity expected in the rotated frame, a correction to this estimate provides the streamwise velocity, $V = V' \cos(\theta)$, where θ is the angle that the image was rotated to align the FLEET line with vertical.

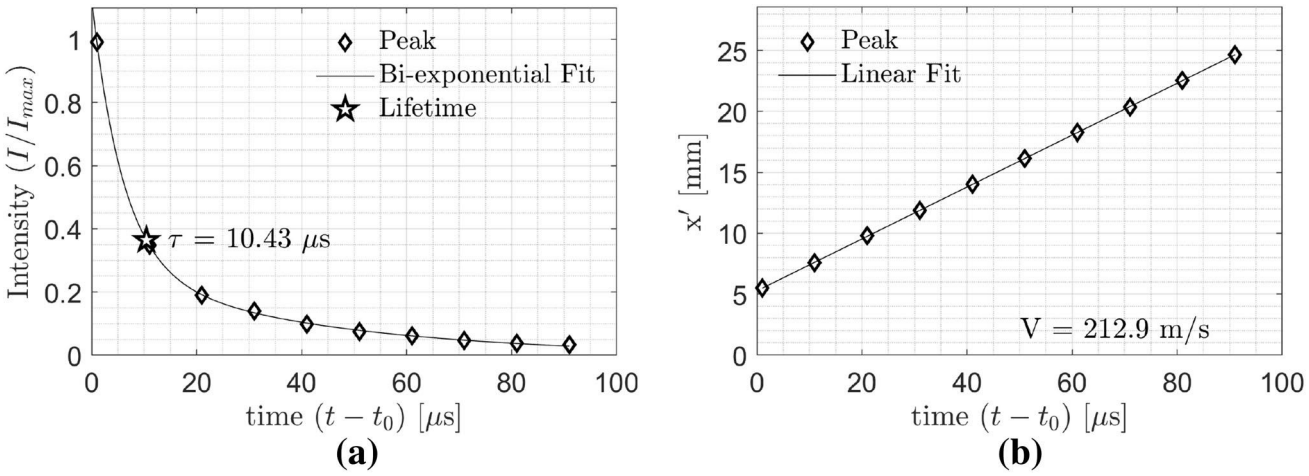

Fig. 3 Typical results exhibiting the methods used to extract **a** FLEET signal lifetime, and **b** flow velocity measurements using fits to normalized peak intensity and position as a function of time

A slight error is known to exist as a result of performing MTV using an angled FLEET signal (Hammer et al. 2013), however, this error is negligible in the current work since only a small angle ($\sim 7°$) was introduced and velocity in the vertical direction was nominally zero. The measured positions of peak FLEET intensity for each exposure are shown as open diamonds in Fig. 3b, while the linear fit in time that provides flow velocity is shown as a solid line. To ensure that only valid and physical results are considered, any fits with $R^2 < 0.97$ were excluded from further analysis; this constraint eliminated approximately 4% of the single-shot data. In the following section, this method of velocimetry is not only proven to provide accurate measurements of freestream flow velocity across a range of tunnel operating conditions but is also shown to enable the extraction of velocity profiles and two-dimensional velocity maps in the wake of the CRM wing.

4 Results

FLEET measurements obtained over a variety of flow conditions and model attitudes are presented within this section; these results represent the first non-intrusive, quantitative measurements of velocity made in NASA's large-scale TCT. In Sect. 4.1, freestream measurements are compared against theory and existing velocity measurements provided by the facility DAS in order to establish baseline performance of the FLEET system in the NTF. Once the application of this method of velocimetry has been proven to provide accurate results, a description of additional processing steps used to produce FLEET velocity profiles is outlined in Sect. 4.2, and profile structure as a function of model angle-of-attack (AOA) is explored. With an understanding of how FLEET velocity profiles are obtained, a method for constructing a two-dimensional velocity map in the wake of the CRM wing is introduced, and representative results demonstrating the typical data quality that can be expected from the system are presented. Finally, the two-dimensional velocity map measured using the FLEET technique is compared against a CFD solution (which also serves to provide additional insight into FLEET measurements) in Sect. 4.3.

4.1 Freestream velocity measurements

Following the extraction of freestream velocity as described in Sect. 3.3, FLEET velocimetry results can be compared against the theoretical values expected given the thermodynamic conditions of the flow. Figure 4a, b shows the freestream velocity measured by the FLEET system as a function of total (stagnation) temperature and total pressure. In each figure, triangular symbols represent the time-averaged velocities obtained in air mode, circles show the average value of the single-shot FLEET measurements taken in nitrogen, and error bars represent the uncertainty in the mean over all valid velocity results considered in the measurement ($U_m = 2\sigma/\sqrt{N}$, where σ is the standard deviation of velocity and N is the number of single-shot velocities included). Dotted lines in Fig. 4a are the theoretical value of velocity associated with specific Mach numbers at each temperature in air, while solid lines indicate $M = 0.8$ and $M = 0.9$ in nitrogen. Figure 4a clearly shows that the FLEET system is sufficiently sensitive to resolve the proper rise in flow velocity accompanying an increase in temperature for any of the Mach numbers tested. Symbols are the same in Fig. 4b, but here the line type indicates the theoretical velocity at each of the four nominal flow temperatures considered for the $M = 0.8$ runs. Figure 4b not only demonstrates that

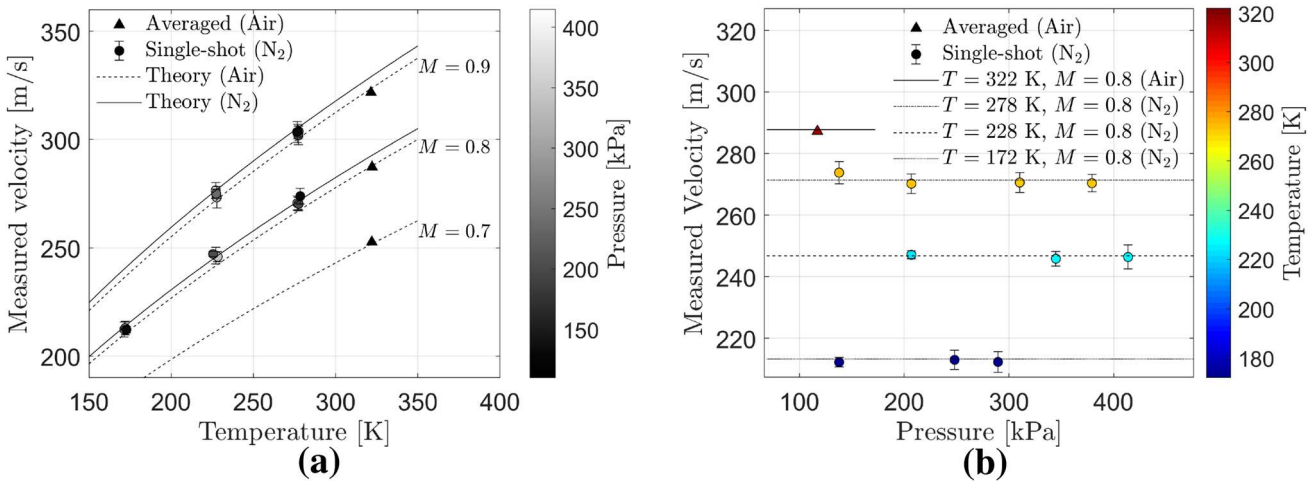

Fig. 4 FLEET results as a function of thermodynamic conditions. Flow velocity measurements are shown in relation to theory as a function of **a** temperature, and **b** pressure

FLEET velocity measurements are independent of pressure (as predicted by isentropic flow theory) but also shows that results agree with theoretical values within U_m for all conditions.

In addition to considering their relation to theoretical solutions, FLEET measurements obtained in the NTF are assessed for accuracy using the facility DAS velocity values as a basis for comparison. This comparison is shown in Fig. 5, where freestream flow measurements made using the FLEET system are plotted against velocity determined by the existing (and completely independent) wind tunnel data system. The solid line in Fig. 5 represents perfect agreement between the two measurement systems, while the dotted lines bound ±2.5% error. Though measurement accuracy for all flow conditions lies within 2.5%, a majority of conditions agree within 1% yielding an average error of 0.87%, similar to accuracies attained in earlier LEET experiments in small-scale TCTs (Burns et al. 2018a, b; Reese et al. 2020).

4.2 Velocity profile measurements

As previously mentioned, a significant improvement in FLEET signal-to-noise ratio (SNR) was achieved in the second experimental campaign relative to the initial

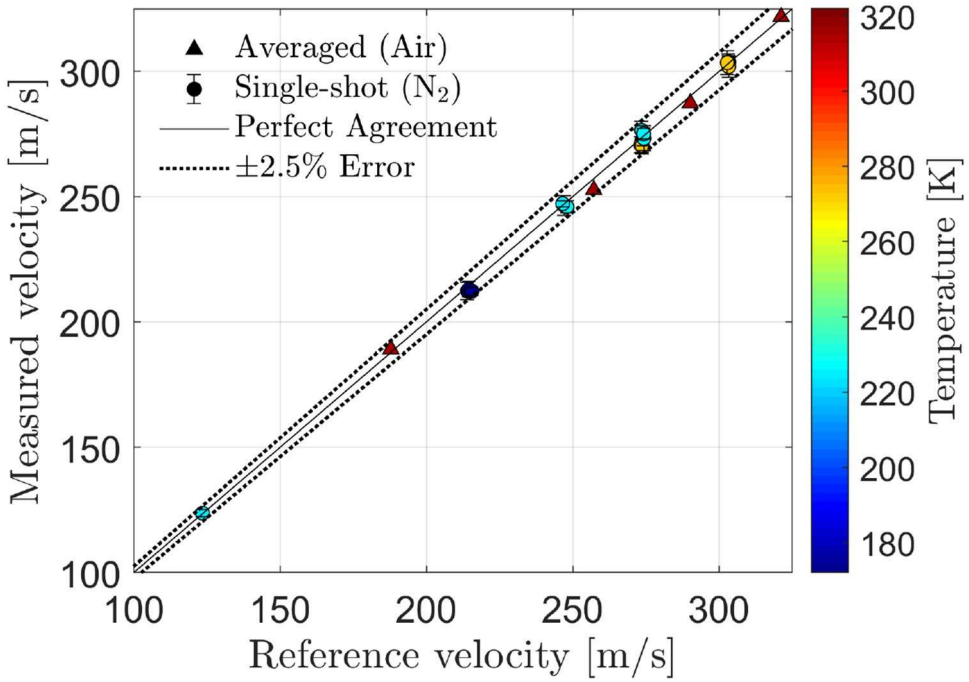

Fig. 5 Accuracy of FLEET velocity measurements compared against values from the tunnel DAS reference. The solid line represents perfect agreement, while the dotted lines indicate ±2.5% error

freestream efforts. The increased SNR is attributable to upgrades to the LPS and optics system (described in the final paragraph of Sect. 2.2) and afforded the ability to calculate spatially resolved velocity profiles along the FLEET line. This was accomplished by first binning each preprocessed FLEET ROI into several bins along the height of the image, rather than a single bin as was done in the analysis of freestream data. A typical ROI image is shown segmented into 12 bins in Fig. 6a. By binning the FLEET signal into multiple rows, SNR is increased to a level sufficient to perform velocimetry while also maintaining spatial resolution in the vertical direction. Similar to the freestream analysis, binned data can then be modeled as a series of Gaussians on noise, although now a total of 12 profiles are fit for each ROI, rather than just one. The 12 FLEET intensity profiles (along with corresponding Gaussian and peak intensity/location fits) are shown in Fig. 6b, where each profile corresponds to a different y' location.

It should be noted here that the number of bins into which the FLEET image is divided must be regarded as a balance between SNR and spatial resolution; a larger number of bins means improved spatial resolution but also lower SNR, and vice versa for fewer bins. Velocity measurement precision was chosen as the defining metric used to determine the size of bins in the present work. By calculating the standard deviation of streamwise velocity measurements (σ_u) as a percentage of freestream velocity (u_x) and plotting this precision as a function of bin size, a clear trend emerges. Figure 6c shows the calculated precision for each bin size as a black dot, while a fit to these data is shown as a solid line. This fit confirms that to first order, the bin size reflects averaging over that number of samples, which results in a reduction in fluctuations by $\sqrt{bin\ size}$. The selected bin size

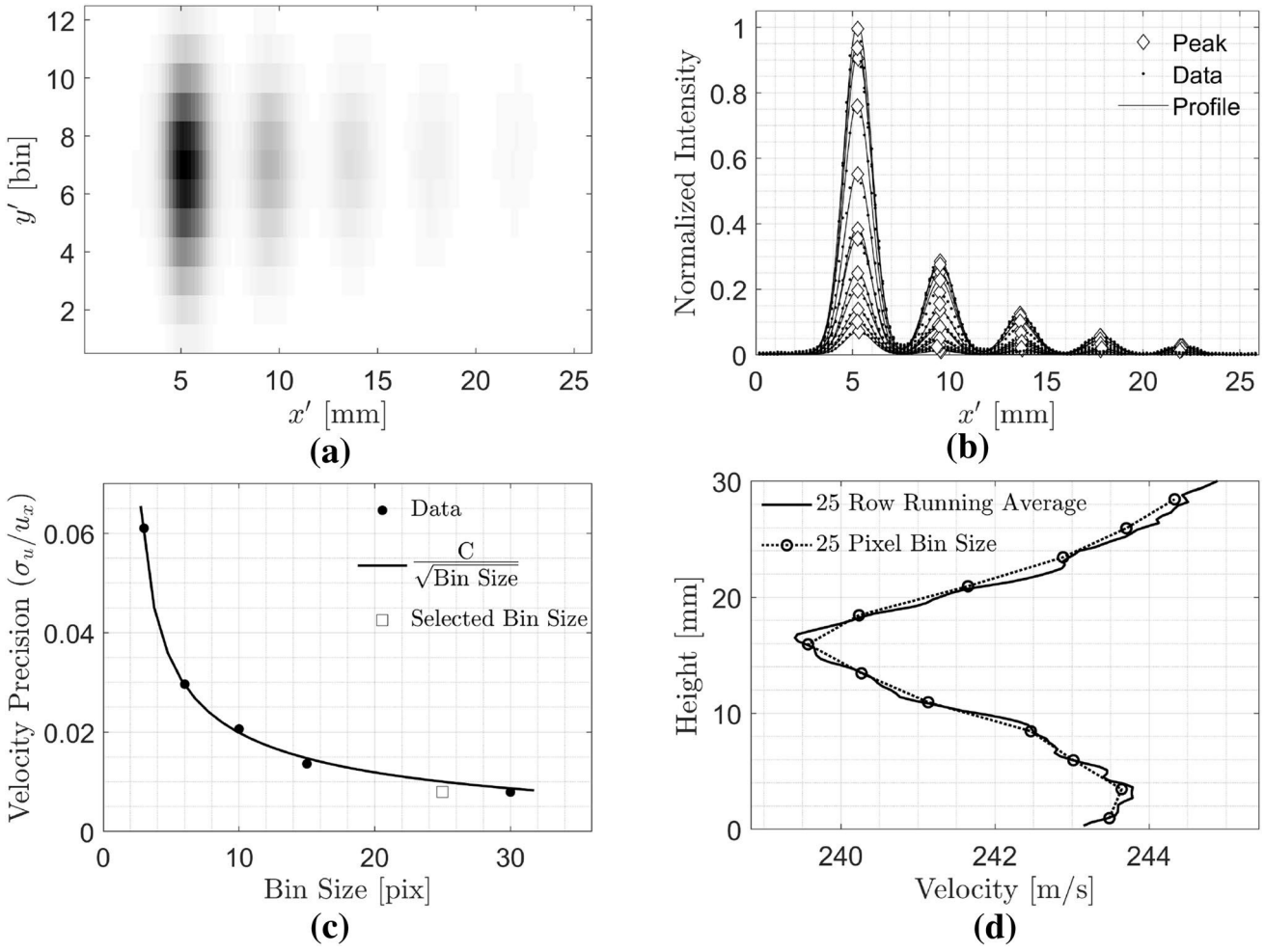

Fig. 6 Typical dataset exemplifying each of the processing steps used to provide velocity profile measurements. **a** 25 pixel binned FLEET region of interest. **b** Intensity profiles for each bin, modeled as a series of Gaussians on noise and fit for the location of peak intensity to sub-pixel accuracy. **c** Velocity measurement precision as a function of bin size. **d** Velocity profiles showing a deficit in the wake region downstream of the CRM wing

of 25 pixels used for further analysis is shown as an open square, which (for a typical FLEET ROI containing approximately 300 pixels in the y' direction) corresponds to 12 bins. This bin size was chosen because it is the smallest bin size that achieves $\sigma_u/u_x < 1\%$, therefore yielding the highest possible spatial resolution while placing measurement precision for this study on order with previous LEET experiments in cryogenic facilities (Burns et al. 2018a, b; Reese et al. 2020).

Using the same processing techniques employed for freestream data analysis, peak fit locations from every profile modeled in Fig. 6b provide a separate velocity measurement for each of the corresponding y' locations. These 12 velocity measurements can then be mapped back to their position within the wind tunnel. Velocity measurements as a function of height are shown as open circles in Fig. 6d, and the dotted line connecting each measurement represents the calculated velocity profile. In order to increase the grid density of the velocity profile while maintaining similar SNR and measurement precision, a 25-row running average was also used to extract profiles, and a typical "high resolution" velocity profile is shown in Fig. 6d as a solid line. Both profiles indicate a clear velocity deficit due to wake effects caused by the CRM wing upstream of the measurement region; however, additional details can be seen in the high resolution profile that have been filtered out by the binning process, including a somewhat stronger velocity deficit occurring at a slightly different height. For simplicity, only the running average velocity profiles will be used throughout the remainder of this report. With an understanding of how FLEET velocity profiles are calculated, the following portion of this subsection is broken into two parts, each highlighting a different application of FLEET profile measurements in the NTF. Part one explores the influence of the CRM attitude on downstream wake structure through observations of profile shape as a function of model AOA. Part two introduces a method for constructing a two-dimensional velocity map from profiles obtained at several different spanwise positions in the tunnel and also offers representative results demonstrating the typical data quality that can be expected from the FLEET velocimetry system.

4.2.1 Velocity profiles versus model AOA

Effects of the CRM attitude on wake velocity profile structure can be probed by changing the model AOA while keeping the FLEET signal stationary in the test section. For this study, velocity profile measurements were taken at the $z = 0$ spanwise position, located approximately 12.7 cm outbound from the leading edge at the tip of the horizontal stablizer. Results of this study are provided in Fig. 7 for an AOA sweep in one-degree increments conducted in air mode at a Mach number of 0.7, total temperature of 322 K, and total pressure of 233 kPa. Velocity profiles for "low AOA" model angles ranging from $-2° < \alpha < 3°$ are shown in Fig. 7a, while Fig. 7b contains profiles for "high AOA" attitudes ranging from $4° < \alpha < 9°$. Figure 7c shows the mean velocity measured for each profile as a function of model angle and clearly displays the reason for selecting $\alpha \approx 3°$ as the natural distinction point between low and high AOA. For $\alpha < 3°$, an increase in AOA causes an overall increase in flow velocity within the measurement region; beyond $\alpha = 3°$, however, further increasing the AOA leads to a reduction in mean velocity. Note that, the minimum velocity deficit occurs near the 3° AOA designed for cruise. As shown in Fig. 7a, the increase in mean velocity at low model angles is due to the presence of a clear velocity deficit peak that exists within the measurement region at negative AOA, but which appears to broaden and trend upward as model angle is increased, until near-freestream conditions are reached at $\alpha \approx 3°$. Velocity profile measurements shown in Fig. 7b appear to indicate that the reduction in mean velocity with increasing AOA at large model angles is due, in part, to the development of a dual-peaked deficit region that broadens with increasing AOA. Further thoughts regarding these wake

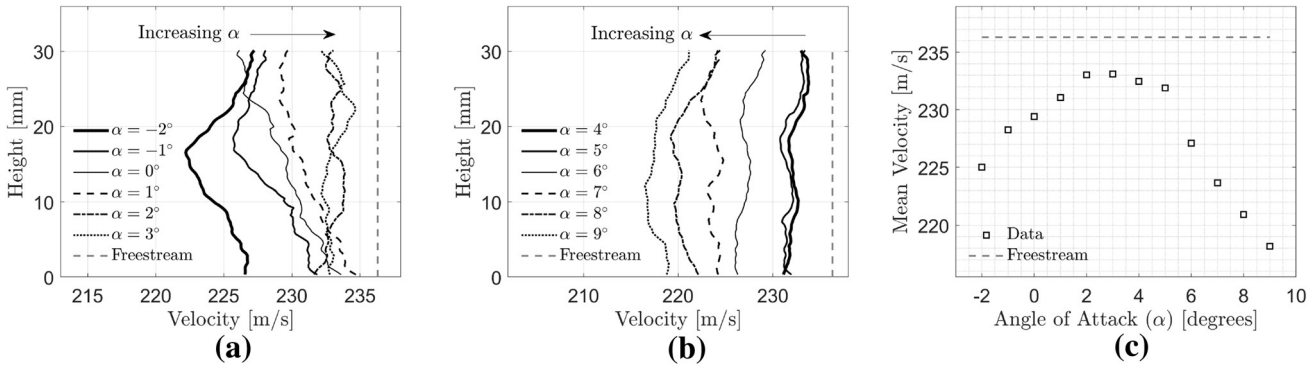

Fig. 7 Velocity measurements in air at various CRM angles of attack for the $M = 0.7$, $T = 322$ K, $P = 233$ kPa case. **a** Low AOA velocity profiles, $-2° < \alpha < 3°$. **b** High AOA velocity profiles, $4° < \alpha < 9°$. **c** Mean velocity as a function of model AOA in 1° increments across the entire range of angles considered in this study

measurements are provided in Sect. 5 after additional context is provided by CFD solutions in Sect. 4.3.

4.2.2 Two-dimensional velocity map

For the second application of FLEET profile measurements in the NTF, the CRM was maintained at a single attitude and the FLEET signal location was traversed across the spanwise direction of the test section to map out a two-dimensional region in the wake of the CRM wing. Spatial scanning of the laser was accomplished by using the final motorized mirror in the optics system to direct the FLEET emission to eight different measurement locations (each just under 13 mm apart, spanning a total of 89 mm) and using the focus ring attached to the objective lens to remotely refocus the imaging system on the signal at each position. While the current system does not permit movement of the FLEET line along the height of the beam, profiles were extended in the vertical direction by rolling the model ±3° while maintaining the desired 2° AOA. In this way, the FLEET line can provide an additional eight velocity profiles in the region above the original measurement locations (for a roll of +3°), as well as eight more profiles below the original measurement region (for a roll of −3°), totaling 24 measured velocity profiles. By combining the three profiles at each spanwise position, a final extended profile measurement can be obtained. While a slight error is introduced as a result of rolling the model (rather than translating it up and down), this error is negligible since the model was only rolled a small angle. Extended profiles are shown for the $M = 0.85$, $T = 322$ K, $P = 210$ kPa case in Fig. 8 as dotted lines, where each color represents a profile measured at a different spanwise position. These velocity profile measurements are shown projected onto the top and bottom of the measurement domain as grey lines to indicate the extent of measured velocity for each profile. Profiles are also projected onto the back-right plane of the domain as dotted grey lines for a comparison of profile shape, along with a solid grey line indicating the spanwise-averaged velocity profile over the entire measurement region. Finally, solid colored lines at each measurement location represent spatially filtered velocity data for each of the measured profiles. Filtered data are calculated using a moving average with a fixed window size of 7.5 mm.

Rather than viewing these measurements as individual line profiles at eight different spanwise positions, these data can instead be replotted as a more intuitive two-dimensional velocity map. By plotting the spanwise position and height within the test section along the x and y axis, respectively, color can be used to indicate the filtered velocity value at each measurement location. This velocity map is shown in Fig. 9a, where the velocity profile measurements are seen as eight columns spanning the width of the image, and the existence of a two-dimensional velocity deficit region is clearly visible. The position of this velocity map is displayed relative to the CRM in Fig. 9b, where the deficit region is clearly shown to be a result of the wake caused by the wing upstream of the measurement location. The height of maximum velocity deficit shows an upward trend with increasing spanwise distance from the model that appears to rise at an angle greater than that of the CRM wing slope; however,

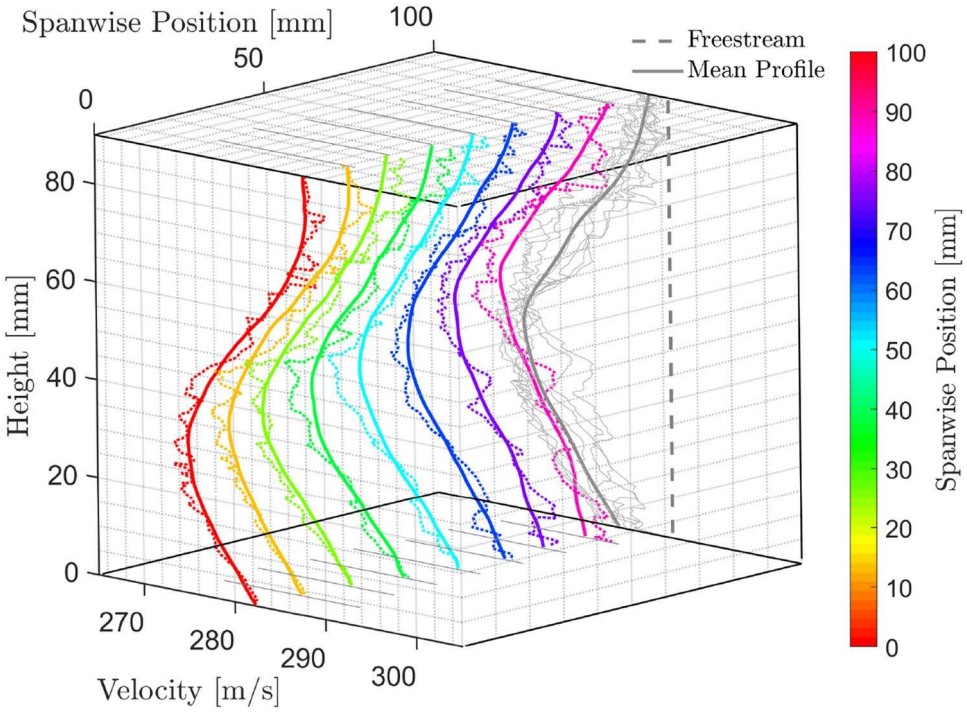

Fig. 8 Extended velocity profiles at each spanwise measurement location are shown as dotted lines, while spatially filtered results are displayed as solid lines. Data shown for the $M = 0.85$, $T = 322$ K, $P = 210$ kPa case in air

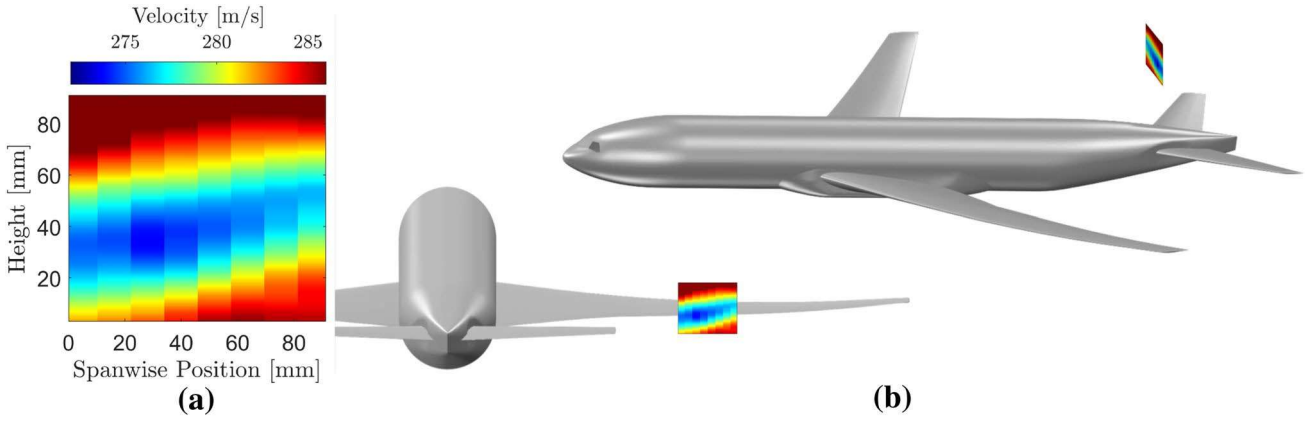

Fig. 9 FLEET measurements in the wake downstream of the CRM wing. **a** Two-dimensional velocity map confirming the existence of a velocity deficit region in the CRM wake. **b** Location of measurements showing results relative to the model

this effect is likely due to model deformation that occurs as the wing is aerodynamically loaded under flight conditions (Burner et al. 1985, 2008). Further context is provided to these wake velocity deficit measurements in the following subsection, where the measured FLEET velocity map is compared directly against a CFD solution. Additionally, a more detailed discussion regarding these FLEET measurements, including a comparison with similar velocimetry results from ETW, is carried out in Sect. 5.

4.3 Comparison with CFD

There is no existing computational solution known to the authors that matches exactly the conditions under which FLEET two-dimensional velocity measurements were made. Resultantly, this subsection considers the most similar case for which a CFD solution exists, and a normalization scheme is applied to allow for comparison between CFD results and experimental measurements. Simulation of flow around the CRM was carried out using USM3D, a tetrahedral unstructured flow solver, as part of the fourth AIAA Drag Prediction Workshop (Vassberg et al. 2010). USM3D is a full viscous Navier-Stokes code with several turbulence models, limiter options, and schemes for computing flux quantities across each cell face. The steady-state CFD solution considered in this work used the Spalart-Allmaras turbulence model, and Roe's Flux-Difference Splitting (FDS) as the upwind flux function. No solution limiter was activated in order to improve skin friction drag prediction. As summarized in Table 1, the test gas, Mach, and chord Reynolds number of the flow, as well as the model geometry and attitude, were identical between CFD and experiment; however, the total temperature of the simulated flow was 255 K, roughly 67 K lower than the experimental value. Additionally, while flow within the wind tunnel is influenced by the test section walls and aerodynamic effects such as vehicle buffeting, the simulation considered only a stationary model in a free-air computational domain. Despite these differences, normalized FLEET measurements made in the wake region downstream of the CRM wing are shown to compare favorably with the normalized CFD solution.

In order to more directly compare experimental results and CFD, the measured FLEET velocity map shown in Fig. 9a was linearly interpolated to match the resolution of the computational solution. The interpolated FLEET velocity map is shown in Fig. 10a, and qualitative

Table 1 Details regarding the CRM model, flow conditions, and domain for the experimental FLEET measurements in NTF and the USM3D numerical simulation

	FLEET measurements	CFD simulation
Model attitude	AOA = 2°, roll = yaw = 0°	AOA = 2°, roll = yaw = 0°
Model config.	WBT0	WBT0
Model motion	Vehicle buffeting and deformation	Deformation only
Test gas	Air	Air
Mach number	0.85	0.85
Reynolds num.	5,000,000	5,000,000
Total temp.	322 K	255 K
Freestream Vel.	285.9 m/s	272.1 m/s
Domain	Slotted test section walls (6% open)	Free (100% open)

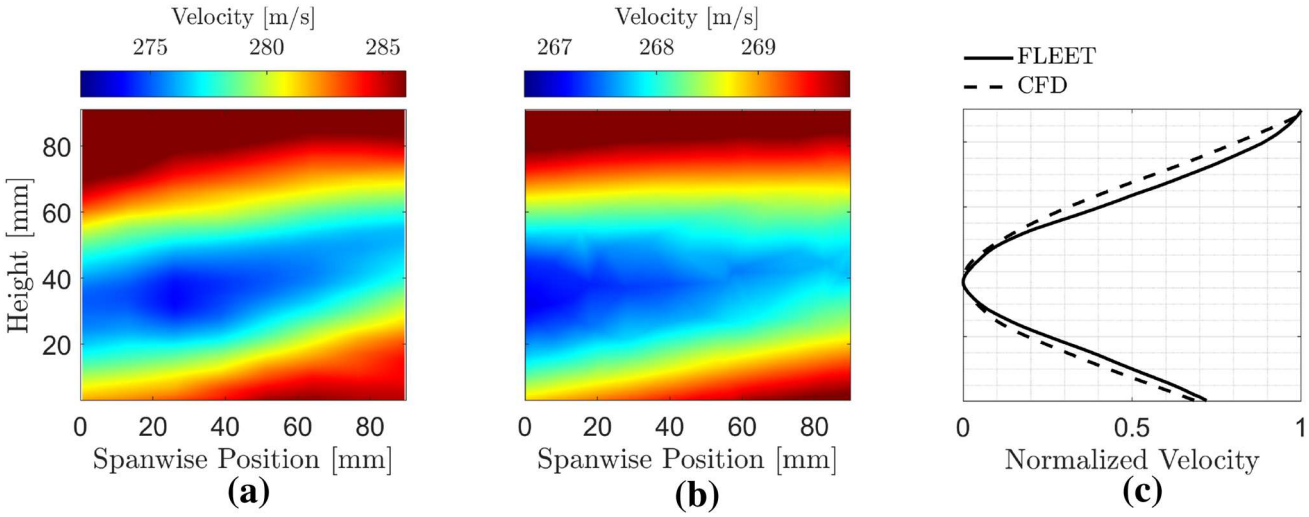

Fig. 10 FLEET velocity measurements compared against CFD. **a** Two-dimensional velocity map showing FLEET measurements interpolated for better comparison with **b** CFD results calculated over the same region. **c** Normalized spanwise-averaged profiles showing comparison between FLEET measurements and CFD solution

similarities to the CFD solution (Fig. 10b) are immediately apparent. With the colorbar of each velocity map appropriately scaled, both results show the existence of a velocity deficit region that rises with increasing distance from the CRM fuselage. A substantial difference between the near-freestream velocity in the region along the top of each image is evident, and results from thermodynamic differences between the CFD and experimental flows. The cooler air considered in the numerical solution causes a nearly 14 m/s reduction in the expected freestream velocity (V_∞); normalizing spanwise-averaged wake profiles by their respective V_∞ allows for comparison between simulation and measurement. Freestream velocity was provided by the facility DAS for FLEET measurements and calculated based on isentropic relations for the CFD solution. Experimental FLEET measurements indicate that the minimum velocity within the wake is approximately $0.95V_\infty$, while the CFD solution estimates a maximum deficit of roughly $0.98V_\infty$. In order to account for these differences and promote further comparison between the two solutions, another normalization scheme is applied to the data which allows for a direct comparison between experimental and computational results. By taking the spanwise average of both velocity maps and normalizing them between 0 and 1 using each profile's minimum and maximum values ($V_{\min}$ and $V_{\max}$), a quantitative comparison between the two can be made. Normalized spanwise-averaged profiles are shown in Fig. 10c, where the location corresponding to $V_{\min}$ for each case is found to agree within the uncertainty of the FLEET measurement location (~ 5 mm), and solutions are shown to match within 10% of $V_{\max}$ across the entire height of the measurement region. Defining the wake thickness to be the extent of the deficit region at the $V_{\text{norm}} = 0.5$ level, FLEET measures a wake 11% thinner than that predicted by CFD. While the different freestream velocities, domains, and model motions considered in each case will account for some of these discrepancies, residual error between the two results may also be partially due to effects such as insufficient measurement integration time and excessive averaging by the computational flow solver.

Further insight into the experimental FLEET measurements obtained in this study can be provided from the computational solution by applying the normalization scheme described above to both datasets. Embedding the normalized velocity map measured by FLEET within the larger normalized CFD solution offers additional context regarding the influence of the surrounding flowfield on the measurement region. This comparison is displayed in Fig. 11 where the CRM model is shown overlaid on the velocity maps, the measurement region is bounded by a dashed line, and fine details in the flow (including effects from the fuselage, wing, and tail) are accentuated by stretching the colorbar beyond unity. Though large-scale features of the FLEET velocity map generally align well with the "big picture" CFD, details along the edges of the measurement region show mismatch between the two solutions. This view also provides an understanding of the general relationship between the wake caused by the CRM wing, the measurement region, and an area of accelerated flow resulting from the presence of the tail (located just above the measurement region for the AOA = 2° case shown in Fig. 11); the effect of each of these flow attributes is considered, and their influence on the features observed in FLEET measurements is covered in the following section.

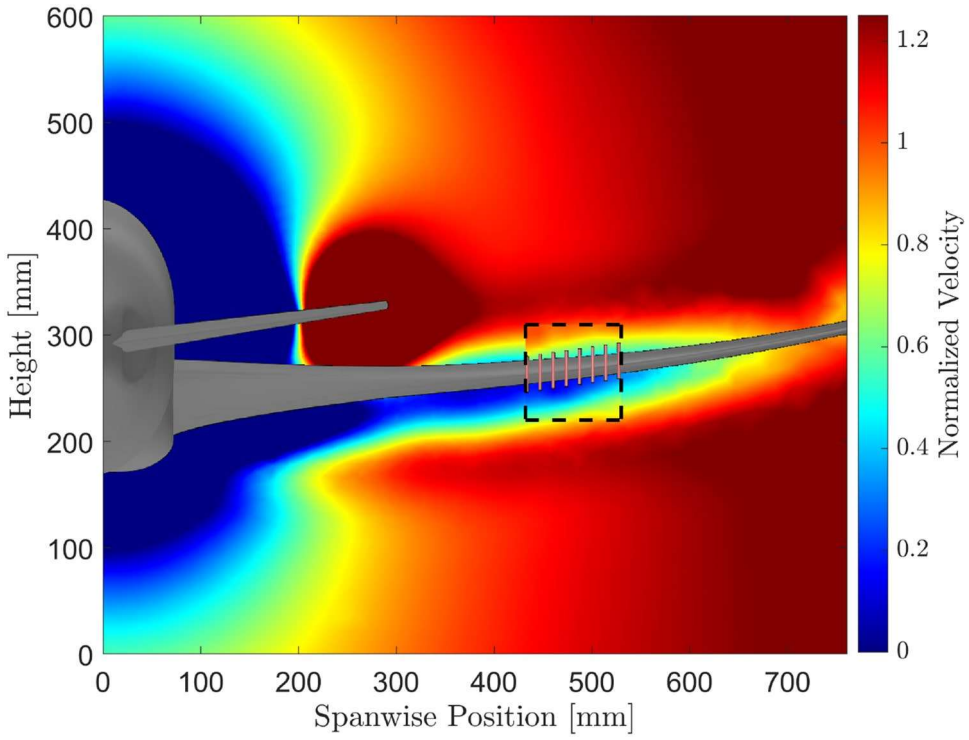

Fig. 11 Normalized CFD solution with model overlay and normalized FLEET velocity map replacing CFD within the measurement region (as outlined by box with dashed lines)

5 Discussion

With a more complete understanding of the experimental results and how they were attained, this section contains an in-depth discussion of the FLEET measurements presented in this report, offers a comparison with similar velocimetry performed in the ETW, and presents final thoughts regarding the significance and future of the newly implemented laser measurement system in the NTF. One important consideration regarding the data presented in the previous section is that FLEET velocity profile measurements were made in warm air; these conditions represent the worst-case scenario in terms of FLEET SNR. Since the FLEET signal improves by nearly 10 times in nitrogen (compared with the oxygen-quenched signal in air) (DeLuca et al. 2014) and also increases at higher density (Burns et al. 2018b), FLEET measurements made at any other conditions within the NTF can expect the benefit of improved emission intensity. This enhanced signal means that preprocessed ROI images may be subdivided into more bins, thereby improving the vertical resolution of the FLEET velocity map while maintaining the necessary SNR for sub-1% precision in velocity measurements. Spatial resolution of the velocity map can also be improved in the horizontal direction by increasing the number of measurement locations along the spanwise direction. For example, the spanwise resolution can be improved twofold by simply scanning the laser to 16 measurement positions every 6.35 mm, rather than the eight locations with 12.7 mm spacing used in the present work.

Despite a significant number of improvements that can be made to ameliorate FLEET measurements in the NTF, the novel results presented herein prove the ability of the laser measurement system to resolve a ~5% effect, providing a two-dimensional velocity map that clearly indicates a deficit in the wake region behind the CRM wing. Though obtained under different flow conditions, these results compare favorably with similar PIV and DGV measurements made in ETW (Lutz et al. 2013; Quest and Konrath 2011; Willert et al. 2005), but with the added benefit of providing *unseeded* flow velocity measurements. Work carried out by Konrath et al. (2015) provided the closest comparison with the research outlined in this report, based on the similarity of both flow conditions and location of the measurement region. Reference Konrath et al. (2015) presents two-dimensional PIV results in the wake of the CRM in ETW (also with a $M = 0.85$ freestream), but at a location upstream and in a plane perpendicular to that measured by FLEET in NTF. Using the same definition of wake thickness introduced in the previous subsection, streamwise velocity at the most downstream location measured by Konrath shows a deficit region approximately 70% the height of that measured in this work. While a majority of this discrepancy is a result of differences in the Reynolds number of the flow and the model AOA, geometric effects also account for some of the variation between measurements. Since wake thickness increases with downstream distance, and PIV measurements were taken upstream of the FLEET measurement region, after accounting for this effect the true difference in wake

thickness between these studies is less exaggerated. The same is true for measurements of velocity deficit in the wake region. While the magnitude of the velocity deficit in reference Konrath et al. (2015) is $0.86V_{max}$, the velocity deficit decreases with downstream distance, implying that current measurements may actually agree better with results presented by Konrath et al. than these initial estimates reflect. Residual disagreement in the wake measurements can be attributed to additional differences in the conditions considered in each study (e.g., total pressure and spanwise measurement location), as well as inertial effects resulting from the use of particulate, rather than molecular, flow tracers.

Other PIV experiments conducted in the ETW also provide two-dimensional velocity measurements in the wake of the CRM (Lutz et al. 2015; Waldmann et al. 2016), and as carried out in Sect. 4.3, results were compared directly against a computational solution. These papers demonstrate a relationship between experimental measurements and CFD which is similar to that observed in this work. In each case, the simulated profiles under predict the value of maximum velocity deficit, while over predicting the wake thickness. Regardless, these CFD solutions can be used to provide additional qualitative information regarding the FLEET measurements made in NTF. For example, CFD shows the presence of an area of accelerated flow resulting from the influence of the CRM tail (see Fig. 11), which may explain trends observed in velocity profile measurements as a function of model AOA. As demonstrated in Fig. 7b, the appearance of a "dual deficit peak" may be a result of the tail-accelerated flow entering the measurement height at large AOA, resulting in a region of increased flow within the larger deficit caused by the CRM wing. Further investigation of this effect—preferably with better-resolved profiles and a computational solution exactly matching the experimental conditions—may be warranted before definitive conclusions regarding the influence of the CRM tail on FLEET profile measurements can be drawn.

While first employed for application of the FLEET technique, it is important to note that the laser measurement system demonstrated in this work was not exclusively developed for (or limited to) femtosecond-laser tagging velocimetry. As designed, any number of pulsed and continuous-wave laser-based diagnostic techniques are capable of utilizing the infrastructure described in Sect. 2; in fact, Rayleigh scattering measurements of density were obtained in conjunction with FLEET velocimetry efforts by simply changing the imaging filter and the timing of the intensifier gates. Although fully functional without further modification, the capabilities of the laser measurement system can be greatly enhanced in future applications through slight additions and alterations to the LPS, optics, and read system. Alignment of the laser within the LPS is currently controlled manually, as is scanning of the FLEET signal within the test section and refocusing of the imaging lens. By automating these tasks, not only is less input and effort required from the researchers, but the time needed to complete a FLEET measurement scan can be greatly reduced, meaning that a larger area or volume can be mapped without additional impact to testing. FLEET signal intensity is also currently diminished as a result of the optics system being exposed to the high-pressure, cryogenic environment within the plenum. Development of an extension to the LPS that acts as an enclosure for the optics system will not only reduce the total path length over which the laser beam quality is degraded through exposure to the harsh conditions inside the wind tunnel, but will also present the opportunity to introduce a vertical scanning system to the experimental setup. The inability to scan the laser along the vertical direction is a significant shortcoming of the current system, however, once this capability is introduced, the measurement region can be moved nearly anywhere within the test section, barring geometrical constraints imposed by the test model, wind tunnel facility, or camera field of view.

6 Conclusions

Unseeded, non-intrusive, off-body, quantitative velocimetry has been performed in a large-scale transonic cryogenic wind tunnel for the first time. These measurements were obtained in NTF using the FLEET technique, which was carried out through the implementation of a novel laser measurement system. The first successful demonstration of the measurement system was carried out in freestream conditions, where measurements showed good agreement with both theory and existing DAS measurements of velocity. While measurement accuracy falls within 2.5% for all flow conditions, typical agreement was found to lie within 1% error. Measurement precision was also determined to fall within 1% of the freestream value, similar to previous LEET experiments in cryogenic facilities. Following this initial campaign to make point measurements in the freestream, one-dimensional velocity profiles and two-dimensional velocity maps were measured in the wake downstream of the CRM wing. Velocity profiles showed an overall increase in mean velocity with increasing AOA, until $\alpha = 3°$, at which point further increase in model AOA lead to a monotonic decrease in mean velocity. Qualitatively, the FLEET velocity map compared favorably against CFD; however, a normalization scheme needed to be applied in order to obtain a quantitative comparison between the two, since no CFD exists that exactly matches the conditions measured in this study. Although sufficiently sensitive to measure a 5% deficit in velocity, a number of improvements to the measurements presented in this work can be made to yield higher-quality results. Some changes that would provide improved results

include conducting FLEET velocimetry at higher pressures and/or lower temperatures, using nitrogen (rather than air) as the test gas, and increasing the measurement resolution along both the height and spanwise direction.

Acknowledgements The authors wish to thank the entire NTF team; without their help these measurements would never have become a reality. Special thanks to Bill Goad, James "Monty" Montgomery, Bill Dressler, Adam Cramer, Roy Neff, and Eric Walker, as well as test engineers Josh Demoss, Scott Goodliff, and Chris Cramer. Additional thanks to Rudy King for allowing us to test out the FLEET system during the rake test, and Melissa Rivers for letting us "piggyback" during the CRM test and providing the CFD solution of flow around the CRM. Thanks also to Peyton Gregory for his assistance in designing the laser penetration system. This work was supported by the NASA Aeronautics Research Mission Directorate Transformational Tools and Technologies project, as well as the NASA Aerosciences Evaluation and Test Capabilities portfolio.

References

Babuska I, Oden JT (2004) Verification and validation in computational engineering and science: basic concepts. Comput Methods Appl Mech Eng 193:4057–4066

Burner AW, Snow WL, Goad WK (1985) Model deformation measurements at a cryogenic wind tunnel using photogrammetry, vol 31. Instrumentation in the Aerospace Industry. ISA, pp 615–622

Burner AW, Goad WK, Massey EA, Goad LR, Goodliff SL, Bissett OW (2008) Wing deformation measurements of the DLR-F6 transport configuration in the National Transonic Facility. AIAA paper 2008-6921

Burns RA, Danehy PM (2017) FLEET velocimetry measurements on a transonic airfoil. In: 55th AIAA aerospace sciences meeting, Grapevine, TX

Burns RA, Danehy PM (2017) Unseeded velocity measurements around a transonic airfoil using femtosecond-laser tagging. AIAA J 55:4142–4154

Burns R, Danehy P, Halls B, Jiang N (2015) Application of FLEET velocimetry in the NASA Langley 0.3 meter transonic cryogenic tunnel. In: 31st AIAA aerodynamic measurement technology and ground testing conference, AIAA-2015-2566

Burns RA, Danehy PM, Halls BR, Jiang N (2016a) Femtosecond laser electronic excitation tagging velocimetry in a transonic, cryogenic wind tunnel. AIAA J 55:680–685

Burns RA, Danehy PM, Peters C (2016b) Multiparameter flowfield measurements in high-pressure, cryogenic environments using femtosecond lasers. In: 32nd AIAA aerodynamic measurement technology and ground testing conference. AIAA Paper 2016-3246

Burns RA, Danehy PM, Jiang N, Slipchenko MN, Felver J, Roy S (2018a) Unseeded velocimetry in nitrogen for high-pressure, cryogenic wind tunnels: part II. Picosecond-laser tagging. Meas Sci Technol 29:075203

Burns RA, Peters CJ, Danehy PM (2018b) Unseeded velocimetry in nitrogen for high-pressure, cryogenic wind tunnels: part I. Femtosecond-laser tagging. Meas Sci Technol 29:115302

Clark AM, Slotnick JP, Taylor N, Rumsey CL (2020) Requirements and challenges for CFD validation within the high-lift common research model ecosystem. AIAA paper no. 2020-2772

Cosner RR (1998) Experimental data needs for risk management in CFD applications. AIAA paper no. 98-2781

Couch JD, Sutanto MI, Witkowski DP, Watkins AN, Rivers MB, Campbell RL (2010) Assessment of the National Transonic Facility for laminar flow testing. AIAA paper no. 2010-1302

Danehy PM, Bathel BF, Calvert N, Dogariu A, Miles RP (2014) Three-component velocity and acceleration measurement using FLEET. In: 30th AIAA aerodynamic measurement technology and ground testing conference, Atlanta, Georgia

DeLuca NJ, Miles RB, Kulatilaka WD, Jiang N, Gord JR (2014) Femtosecond laser electronic excitation tagging (FLEET) fundamental pulse energy and spectral response. In: 30th AIAA aerodynamic measurement technology and ground testing conference, Atlanta, GA

Edwards MR, Dogariu A, Miles RB (2015) Simultaneous temperature and velocity measurement in unseeded air flows with femtosecond laser tagging. AIAA J 53:2280–2288

Fey U, Konrath R, Kirmse T, Ahlefeldt T, Kompenhans J, Egami Y (2010) Advanced measurement techniques for high Reynolds number testing in cryogenic wind tunnels. In: 48th AIAA aerospace sciences meeting including the new horizons forum and aerospace exposition, Orlando, FL. AIAA-2010-1301

Foster JM, Adcock JB (1996) Users guide for the National Transonic Facility research data system. NASA technical memorandum TM-110242

Fuller DE (1981) Guide for users of the National Transonic Facility. NASA technical memorandum TM-83124

Gartenberg E, Weinstein LM, Lee EE (1994) Aerodynamic investigation with focusing schlieren in a cryogenic wind tunnel. AIAA J 32(6):1242–1249

Gartrell LR, Gooderum PB, Hunter WW, Meyers JF (1981) Laser velocimetry technique applied to the Langley 0.3 m transonic cryogenic tunnel. NASA technical memorandum TM-81913

Germain E, Quest J (2005) The development and application of optical measurement techniques for high Reynolds number testing in cryogenic environment. In: 43rd AIAA aerospace sciences meeting and exhibit, Reno, NV

Green J, Quest J (2011) A short history of the European transonic wind tunnel ETW. Prog Aerosp Sci 47(5):319–368

Goodyer MJ (1992) The cryogenic wind tunnel. Prog Aerosp Sci 29(3):193–220

Hammer P, Pouya S, Naguib A, Koochesfahani M (2013) A multi-time-delay approach for correction of the inherent error in single-component molecular tagging velocimetry. Meas Sci Technol 24:105302

Herring GC, Shirinzadeh B (2002) Flow visualization of density in a cryogenic wind tunnel using planar Rayleigh and Raman scattering. NASA technical memorandum TM-2002-211630

Herring GC, Lee JW, Goad WK (2015) Feasibility of Rayleigh scattering flow diagnostics in the National Transonic Facility. NASA technical memorandum TM-2015-218800

Honaker WC, Lawing PL (1985) Measurements in the flow field of a cylinder with a laser transit anemometer and a drag rake in the Langley 0.3 m transonic cryogenic tunnel. NASA technical memorandum TM-86399

Hunter WW, Gartrell LR, Honaker WC (1982) Some NTF laser velocimeter installation and operation considerations. NASA report CP-2243

Jiang N, Halls BR, Stauffer HU, Danehy PM, Gord J, Roy S (2016a) Selective two-photon absorptive resonance femtosecond-laser electronic excitation tagging velocimetry. Opt Lett 41:2225–2228

Jiang N, Halls BR, Stauffer HU, Danehy PM, Gord J, Roy S (2016b) Selective two-photon absorptive resonance femtosecond-laser electronic-excitation tagging (STARFLEET) velocimetry in flow and combustion diagnostics. In: 32nd AIAA aerodynamic measurement technology and ground testing conference, Washington, DC

Jiang N, Stauffer HU, Roy S, Danehy PM, Halls BR, Gord J (2016c) Nitrogen molecular-tagging velocimetry techniques using ultrashort-pulse lasers. In: Proceedings of the laser applications to chemical, security and environmental analysis, Heidelberg, Germany

Jiang N, Mance JG, Slipchenko MN, Felver JJ, Stauffer HU, Yi T, Danehy PM, Roy S (2017) Seedless velocimetry at 100 kHz with picosecond-laser electronic-excitation tagging. Opt Lett 42:239–242

Kilgore RA (1976) Design features and operational characteristics of the Langley 0.3-meter transonic cryogenic tunnel. NASA technical note TN-D-8304

King RA, Andino MY, Melton L, Eppink J, Kegerise A (2014) Flow disturbance measurements in the National Transonic Facility. AIAA J 52(1):116–130

Konrath R, Geisler R, Agocs J, Otter D, Ehlers H, Philipp F, Quest J (2015) High-speed PIV applied to wake of NASA CRM model in ETW under high re-number stall conditions for sub- and transonic speeds. In: 53rd AIAA aerospace sciences meeting, Kissimmee, FL

Ladson CL, Ray EJ (1987) Evolution, calibration, and operational characteristics of the two-dimensional test section of the Langley 0.3 meter transonic cryogenic tunnel. NASA technical publication TP-2749

Li B, Zhang D, Liu J, Tian Y, Gao Q, Li Z (2019) A review of femtosecond laser-induced emission techniques for combustion and fow feld diagnostics. Appl Sci 9:1906

Limbach CM, Miles RB (2017) Rayleigh scattering measurements of heating and gas perturbations accompanying femtosecond laser tagging. AIAA J 55:112–120

Lutz T, Gansel PP, Godard JL, Gorbushin A, Konrath R, Quest J, Rivers SM (2013) Going for experimental and numerical unsteady wake analyses combined with wall interference assessment by using the NASA CRM model in ETW. In: 51st AIAA aerospace sciences meeting, new horizons forum and aerospace exposition, Grapevine, Texas

Lutz T, Gansel PP, Waldmann A, Zimmermann DM, Schulte am Hülse S (2015) Time-resolved prediction and measurement of the wake past the CRM at high Reynolds number stall conditions. In: 53rd AIAA aerospace sciences meeting, Kissimmee, Florida. AIAA 2015-1094

Michael JB, Edwards MR, Dogariu A, Miles RB (2011) Femtosecond laser electronic excitation tagging for quantitative velocity imaging in air. Appl Opt 50(26):5158–5162

Oberkampf WL, Trucano TG (2000) Validation methodology in computational fluid dynamics. AIAA paper 2000-2549

Oberkampf WL, Trucano TG (2002) Verification and validation in computational fluid dynamics. Prog Aerosp Sci 38:209–272

Oberkampf WL, Barone MF (2004) Measures of agreement between computation and experiment: validation metrics. AIAA paper 2004-2626

Peters CJ, Shneider MN, Miles RB (2019) Kinetics model of femtosecond laser ionization in nitrogen and comparison to experiment. J Appl Phys 125:243301

Quest J, Konrath R (2011) Accepting a challenge—the development of PIV for application in pressurized cryogenic wind tunnels. In: 41st AIAA fluid dynamics conference and exhibit, Honolulu, HI

Ray EJ, Ladson CL, Adcock JB, Lawing PL, Hall RM (1979) Review of design and operational characteristics of the 0.3-meter transonic cryogenic tunnel. NASA technical memorandum TM-80123

Reese DT, Burns RA, Danehy PM, Walker EL, Goad WK, (2019) Implementation of a pulsed-laser measurement system in the National Transonic Facility. AIAA Aviation Forum 2019. Dallas, Texas

Reese DT, Danehy PM, Jiang N, Felver J, Richardson D, Gord J (2019) Application of resonant femtosecond tagging Velocimetry in the 0.3-meter transonic cryogenic tunnel. AIAA J 57:3851–3858

Reese DT, Danehy PM, Jiang N, Felver J, Richardson D, Gord J (2018) Application of STARFLEET velocimetry in the NASA Langley 0.3 meter transonic cryogenic tunnel. In: AIAA aerodynamic measurement technology and ground testing conference, Atlanta, GA

Reese DT, Jiang N, Danehy PM (2020) Unseeded velocimetry in nitrogen for high-pressure, cryogenic wind tunnels: part III. Resonant femtosecond-laser tagging. Meas Sci Technol 31:075203

Retter JE, Burns RA, Fisher JM, Felver JJ, Reese DT, Danehy PM (2021) On the use of liquid nitrogen droplets as flow tracers in cryogenic flow facilities at NASA Langley Research Center. AIAA SciTech forum and exposition, Nashville, Tennessee

Shirinzadeh B, Herring GC, Barros T (1999) Demonstration of imaging flow diagnostics using Rayleigh scattering in Langley 0.3-m transonic cryogenic tunnel. NASA technical note TN-1999–208970

Snow WL, Burner AW, Goad WK (1982) Image degradation in Langley 0.3 meter transonic cryogenic tunnel. NASA technical memorandum TM-84550

Snow WL, Burner AW, Goad WK (1987) Improvement in the quality of flow visualization in the Langley 0.3-meter transonic cryogenic tunnel. NASA technical memorandum TM-87730

Vassberg J, Dehaan M, Rivers M, Wahls R (2008) Development of a common research model for applied CFD validation studies. In: 26th AIAA applied aerodynamics conference AIAA paper 2008-6919

Vassberg JC, Tinoco EN, Mani M, Rider B, Zickuhr T, Levy DW, Brodersen OP, Eisfeld B, Crippa S, Walls RA, Morrison JH, Mavriplis DJ, Murayama M (2010) Summary of the fourth AIAA CFD drag prediction workshop. In: 28th AIAA applied aerodynamics conference AIAA paper 2010-4547

Viehweger G (1989) The Kryo-Kanal Koln (KKK): description of the tunnel conversion, thermal insulation, instrumentation, operational experience, test results and operating costs. Advisory Group for Aerospace Research and Development (AGARD) CP-744, paper 4

Wahls RA (2001) The National Transonic Facility: a research retrospective. In: 39th AIAA aerospace sciences meeting and exhibit, Reno, Nevada, AIAA-2001-0754

Waldmann A, Gansel PP, Lutz T, Krämer E (2016) Unsteady wake of the NASA common research model in low-speed stall. J Aircr 53(4):1073–1086

Wegener PP (1991) Cryogenic transonic wind tunnels and the condensation of nitrogen. Exp Fluids 11(5):333–338

Willert C, Stockhausen G, Beversdorff M, Klinner J, Lempereur C, Barricau P, Quest J, Jansen U (2005) Application of Doppler global velocimetry in cryogenic wind tunnels. Exp Fluids 39:420–430

Zhang Y, Miles RB (2018) Femtosecond laser tagging for velocimetry in argon and nitrogen gas mixtures. Opt Lett 43:551–554

Zhang Y, Danehy PM, Miles RB (2018) Femtosecond laser tagging in 1, 1, 1, 2-tetrafluoroethane with trace quantities of air. In: 53rd AIAA aerospace sciences meeting, Kissimmee, FL